Published in Journal of Atmospheric and Solar-Terrestrial Physics
Vol. ??, N. ??, pp.?????, 2010.
Doi:10.1016/j.jastp.2010.06.011

A case study of the evolution of a Kelvin-Helmholtz wave and turbulence in noctilucent clouds

P. Dalin[a,b,*], N. Pertsev[c], S. Frandsen[d], O. Hansen[e], H. Andersen[e], A. Dubietis[f], R. Balciunas[f]

[a] Swedish Institute of Space Physics, Box 812, SE-981 28 Kiruna, Sweden
[b] Space Research Institute, RAS, Profsouznaya st. 84/32, Moscow 117997, Russia
[c] A.M. Obukhov Institute of Atmospheric Physics, RAS, Pyzhevskiy per. 3, Moscow 119017, Russia
[d] University of Aarhus, Ny Munkegade, Bygn. 1520, DK-8000 Aarhus C, Denmark
[e] The Danish Association for NLC Research, Lyngvej 36, Kolvrå, DK-7470 Karup J., Denmark
[f] Department of Quantum Electronics, Vilnius University, Sauletekio ave. 9, bldg.3, LT-10222 Vilnius, Lithuania

*Corresponding author at: Swedish Institute of Space Physics, Box 812, SE-981 28 Kiruna, Sweden. Fax: +46 980 79050. E-mail address: pdalin@irf.se (P. Dalin).

Abstract

Bright and extensive noctilucent clouds (NLC) were observed in Århus (Denmark) on 3/4 July of 2008 with an automatic digital camera taking images every minute. This event was unique in the sense that bright NLC were seen at high elevation angles (more than 30 degrees) that allowed observing the evolution of a Kelvin-Helmholtz (KH) wave, resulted in well-developed turbulence. In particular, coherent vortex structures of a horseshoe-shaped form were observed for the first time in noctilucent clouds. The turbulent diffusion coefficient and turbulent energy dissipation rate around the mesopause are estimated in the range of 162-667 m^2/s and 300-1235 mW/kg, respectively, representing a case of strong neutral air turbulence in noctilucent clouds. Turbulent structures were observed to be in the vicinity of breaking small-scale gravity waves that seems to be responsible for a high level of turbulence.

At the same time, it has been demonstrated that it is of importance to take into account non-turbulent process such as the gravity wave motion that is always present in NLC layers. Unless non-turbulent process is taken into account, this certainly leads to overestimating of the value of the turbulent diffusion coefficient. More accurate characteristics of turbulence in NLC can be obtained by analyzing a sequence of high-resolution images with a high frame-rate high-resolution digital camera.

Keywords: Noctilucent clouds, Atmospheric turbulence, Mesospheric dynamics

1. Introduction

Noctilucent clouds (NLC) are the highest clouds in the Earth's atmosphere, observed close to the mesopause in the 80–90 km altitude range. These clouds are a beautiful night-time optical phenomenon occurring during the summer months at mid- and high latitudes. NLC consist of water ice particles of 30–100 nm in radius that scatter sunlight and thus NLCs are readily seen against the dark twilight arc from May until September (Gadsden and Schröder, 1989).

NLC almost always exhibit a wave surface represented by a complex interplay of gravity waves of small-, medium- and large scales. Small-scale billow waves with wavelength of 5-10 km (similar to that of billows in tropospheric clouds) are caused by wind shear around the mesopause (Hines, 1968; Haurwitz and Fogle, 1969; Grishin and Kurilova, 1973; Kuhnke, 1976). These billow waves represent the Kelvin-Helmholtz instability which is a common phenomenon in the lower and middle atmosphere (Fritts and Rastogi, 1985). Sometimes one can see dark holes which seem to be signatures of turbulent processes around the mesopause (Witt, 1962).

The KH instability has been numerously investigated with analytic techniques (for example, Drazin, 1970; Kelly and Maslowe, 1970; Corcos and Sherman, 1976), numerical simulations (for example, Tanaka, 1975; Patnaik et al., 1976; Peltier et al., 1978; Fritts, 1982; Palmer et al., 1996) as well as in laboratory studies (Thorpe, 1968, 1971, 1973; Scotti and Corsos, 1972; Browand and Winant, 1973). Characteristics of KH waves have been obtained in the atmosphere with tropospheric and noctilucent cloud observations (Witt, 1962; Ludlam, 1967; Haurwitz and Fogle, 1969) and radar measurements (Hicks and Angell, 1968; Gossard et al., 1971; Browning and Watkins, 1970).

In spite of a wealth of information on theoretical and laboratory studies of the KH-wave, we could not find in literature a detailed description on evolution of the KH-wave in NLC. The purpose of the present paper is to trace in detail a formation, development and decay of a KH wave and successive turbulence in NLC. Also, for the first time we demonstrate that using a simple time lapse photographic technique it is possible to estimate correctly the turbulent diffusion coefficient (taking into account the wave motion) by tracing the changes of turbulent areas associated with a KH wave.

2. The technique used

In order to estimate the dynamical parameters of NLC in three-dimensional space from photographs, one needs observations made from two points. Unfortunately, in the present case we have only a single point observation from Aarhus (Denmark). Nevertheless we can estimate dynamical characteristics in a horizontal plane because the altitude range of NLC is well known. The previous photogrammetric works (Burov, 1959; Witt, 1962) and present lidar observations (Nussbaumer et al., 1996) show that the majority of NLC are quite stable in altitude and vary between 80 and 85 km. Thus, it is adequate to use the median value of 82.9 km (Gadsden and Schröder, 1989) to estimate the NLC characteristics in the horizontal plane. Uncertainty of 2 km in altitude yields a small relative error of 2-3% in calculating of the horizontal extent of the NLC fine structure and its velocity. The velocity of the NLC detail is defined by its displacement during the time between two successive images taken in one minute. The photogrammetric measurements have been performed by using the positions of the stars, which are the most precise reference points to determine elevation and azimuthal angles of a selected object. The elevation angle of an object has been corrected for atmospheric refraction since NLC are observed at low angles above the horizon; the Laplace formula has been used for calculation of

astronomical refraction. The projection of the NLC detail has been made on the spherical earth taking into account the dependence of the meridional and normal radius of curvature on latitude of a projected point. Also, the elevation of the observation point above sea level has been taken into account. The mathematical description of this technique can be found in Dalin et al. (2004).

3. The features of the analyzed NLC display

A bright and extensive NLC were observed on 3/4 July of 2008 by the automatic NLC camera placed in Aarhus (Denmark). This camera is one of the six cameras located along the same latitude band (54-56°N) around the globe. Each camera operates from the end of May until middle of August and takes images every 1 minute in night time during high NLC season (June 10 – July 25). The detailed description of the network of NLC cameras and operation schedule is given by Dalin et al. (2008). The interested reader is recommended to download the original images as well as the movie to look in detail at the studied NLC display from the following Internet resource:

ftp://ftp.irf.se/pub/tmp/outgoing/pdalin/NLC/DENMARK/2008/2008-07-04/

Further we keep the numbering of the original images to allow the reader to compare images considered in the paper with original ones.

Note the following features inherent to this display, please refer to both Plate 1 and the series of images available on the website for comprehensively understanding of the NLC motions. The bulk of NLC field was moving NE to SW at rather high apparent speed. The NLC field was extended both from north to south and from east to west, and covered almost all the available area of the image (55.7×41.8°) between 03:00 and 04:00 LT, with the veil modulated by wave systems of bands and billows. The last point is of importance for considerations presented below. Long stationary (relative to the ground) bands of 100-170 km length were also seen at about 4-8° above the horizon with a wavelength of 25-30 km, with other shorter bands and billows passing visually through the stationary waves, representing likely multiple layers of NLC.

The present display was characterized by rather large speeds of the motion varying from 59 to 165 m/s. The measured points and their speeds are marked in Plate 1 (Image 274). Note that such high speeds of NLC were typically observed when the clouds were seen coming from the north or northeast (Gadsden and Schröder, 1989). Also note that the velocities of NLC were found to vary from 18 to 262 m/s in a large number of observations by Burov (1967).

The dark holes were seen from time to time (see Plates 2 and 3) close to billow crests as well as slightly apart of crests. In the present case we could observe such hole patterns at high elevation angles from 33 to 38° (the upper limit of the image bound), which is a big advantage of the regarded case since one can measure with a good accuracy their spatial scales (spatial resolution of the image at elevation angle of 35° is 135 meters) as well as trace their appearance and disappearance and be sure that such hole patterns are not caused by superposition of small-scale waves. Similar holes were observed by Witt (1962) but he could not deduce their properties due to their location at low elevation; at the same time he suggested that such patterns might be caused by small-scale turbulence.

Images 275-279 as well as 287 and 288 illustrate a very interesting feature of turbulence regime, namely, occurrence of horseshoe-shaped vortex structures. We could not find a description in literature of such structures in noctilucent clouds and therefore we are supposedly observing them for the first time in NLC. Description of these structures will be given later in the Discussion.

Plate 1 (Image 274). The NLC display seen in Aarhus (Denmark) on 3/4 July 2008. Points show the ground speed (m/s) of the NLC details. The dashed area is analyzed in detail. The field of view of the image is 55.7×41.8°; the field of view of the dashed area is 21.2×9.4°.

4. Analysis of the evolution of the Kelvin-Helmholtz wave

The formation, development and decay of the Kelvin-Helmholtz waves have been observed at high elevation angles (between 33 and 38°) in the images 270-279 (Plate 2) during 9 minutes. The area analyzed with the KH billows is bounded by the dashed line in Image 274. The life cycle of the KH billows and successive turbulence in NLC are very similar to the laboratory experiment performed by Thorpe (1971) (their Fig. 5), which are compared in details step by step below.

1. The wide crests of low intensity (due to small wave amplitude and hence low optical depth) appear on the enlarged parts of Images 270 and 271; similar characteristics of a forming wave appear on the Panels from A to D of Fig. 1.
2. The crests become narrower and brighter (Images 272, 273, 274, 275) due to the increasing of wave amplitude and hence due to increase of optical depth (note that we look at the billows from below and at high elevation angle). Similar increase of wave amplitude and narrowing of width of the KH wave in the laboratory experiment are seen on Panels C, D, E and F of Fig. 1. The relative brightness variations of most pronounced two NLC billows are shown in Fig. 2. The relative brightness of the billows was estimated by subtracting average digital background brightness from average digital brightness of the billows. The brightness

continuously increases during first 5-6 minutes and then starts to oscillate around a mean value due to the saturation of the NLC brightness (limited by the number of ice particles in a wave crest along the line of sight). Note that after 5-6 minutes, the billows are observed to be represented by splintered curves. The variation of brightness of the NLC billows is in a good agreement with the variation of density and horizontal velocity of the billows' environment in the laboratory experiment by Thorpe (1973) (Fig. 12), which demonstrates an increase of the density and velocity through billows at the initial stage, and then density and velocity oscillations due to turbulent areas.

3. Image 273 shows the bifurcation of the first (upper) billow at its end. The same structure is observed in the laboratory billows viewed in the spanwise direction (Figs. 1F and 1G). The billow waves move with slower ground speed compared to ambient areas of NLC. The ground speed of the KH-waves is between 88 and 97 m/s whereas neighbouring areas of NLC move with ground speeds of 120-160 m/s (see Image 274). Thus there is at least a horizontal wind shear in the area containing the billows.
4. The wavelength of the billow waves lies between 10 and 12 km. Such wavelengths are typical for NLC waves caused by the wind shear (Hines, 1968; Grishin and Kurilova, 1973; Gadsden and Schröder, 1989). The lifetime of this system of billows is about 6-7 minutes which are typical life times of NLC billows (Haurwitz and Fogle, 1969).
5. Two dark holes (marked by 3 and 4), bounded by horseshoe-like loops, occur at the two billows (Images 275 and 276) which are signatures of formation of coherent vortical structures; diameter of these vortices is 1650 m and 2400 m, respectively. Note that these two holes (3 and 4 in Image 275) are not chaotically located but oriented along the same line perpendicular to the wave phase front. A similar loop, represented by the dark rounded structure, occasionally occurred at the edges of laboratory billows viewed in the spanwise direction (in the middle of Fig. 1H). Another two larger horseshoe-like loops (marked by 5 and 6 in Images 276 and 277) occur at the top of the two billows; diameter of these structures is 3550 m and 4600 m, respectively. Also, Images 275 and 276 demonstrate at least two jets and two arcs, comprised by NLC particles, originated from the billows and oriented approximately in opposite direction to the apparent motion of the billows (see Fig. 3). These NLC jets and arcs are the unstable parts of the KH wave.
6. The continuous regular billows are fragmented in Images 277, 278, 279 leaving a mixture of the splintered curves, vorticity structures of 1.5-4.6 km in diameter as well as chaotic lacerated dark spots all of which are the signatures of well-developed turbulence. Laboratory billows become wider with lacerated edges; a turbulent mixture is seen between billows (Figs. 1I and 1J). Brightness of NLC splintered curves starts to oscillate around a mean value that is in agreement with the variation of density and horizontal velocity through billows in the laboratory experiment by Thorpe (1973). At the same time, turbulent area with splintered curves, dark patches and vorticity structure in Images 278 and 279 resembles mainly the turbulent field after the breaking of a KH billow in 3-D simulations by Palmer et al. (1996) and Werne and Fritts (2001).

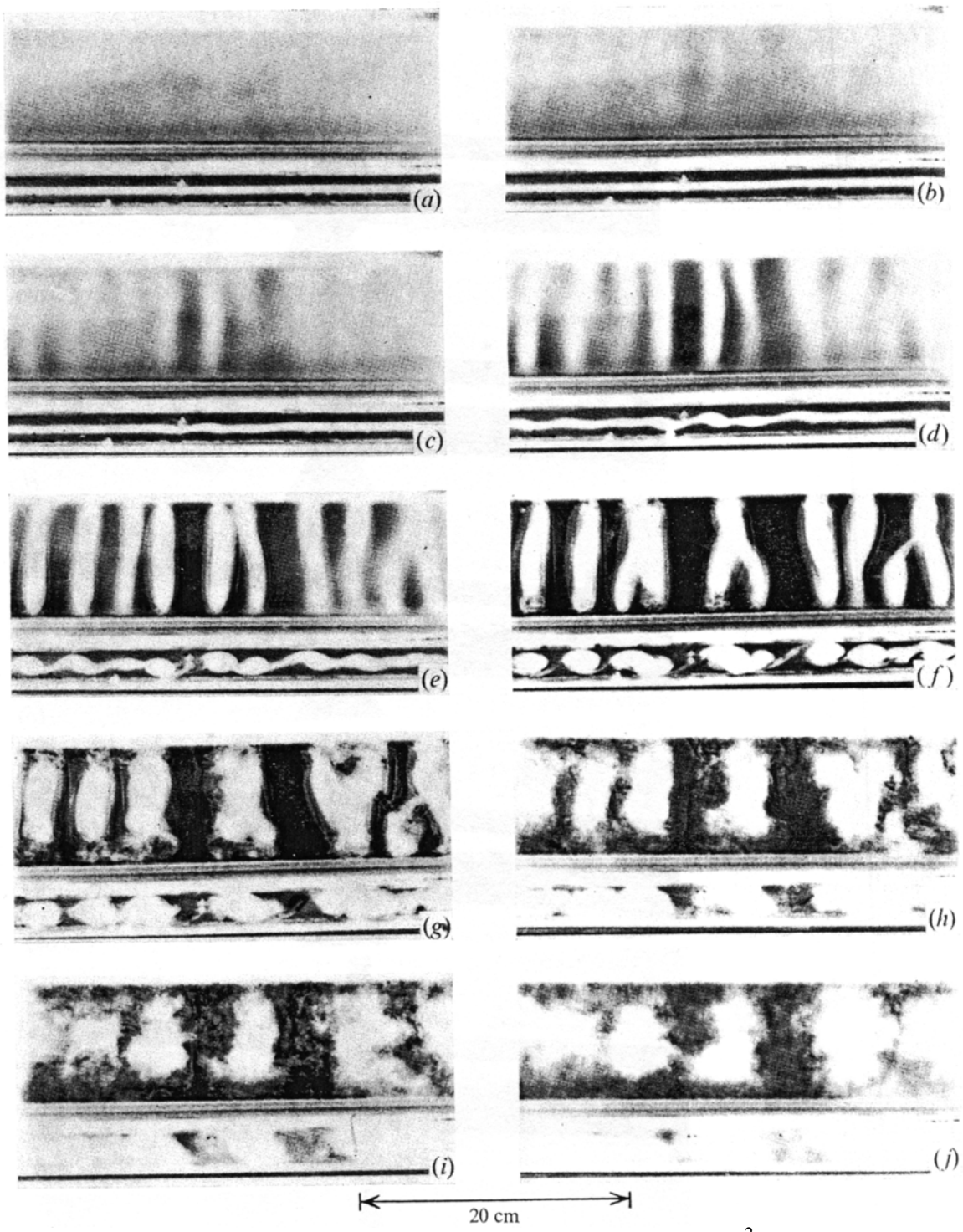

Fig. 1. Instability at the interface between water and brine with $\Delta=2.9\cdot10^{-2}$ g/cc having a layer of dye at the interface. The photographs are taken from a 16 mm ciné film and are in negative so that the dye appears white. The upper part of each shows the plane view as seen through a mirror arranged at 45° to the horizontal and the lower part is a direct view. The tube has an internal cross-section of 3×10 cm. The first photograph is taken at 2.5 sec after tube has been tilted through 8.2°, and subsequent photographs are taken at 0.2 sec intervals. From Thorpe (1971), their Fig. 5 (Reproduced with permission of Cambridge University Press).

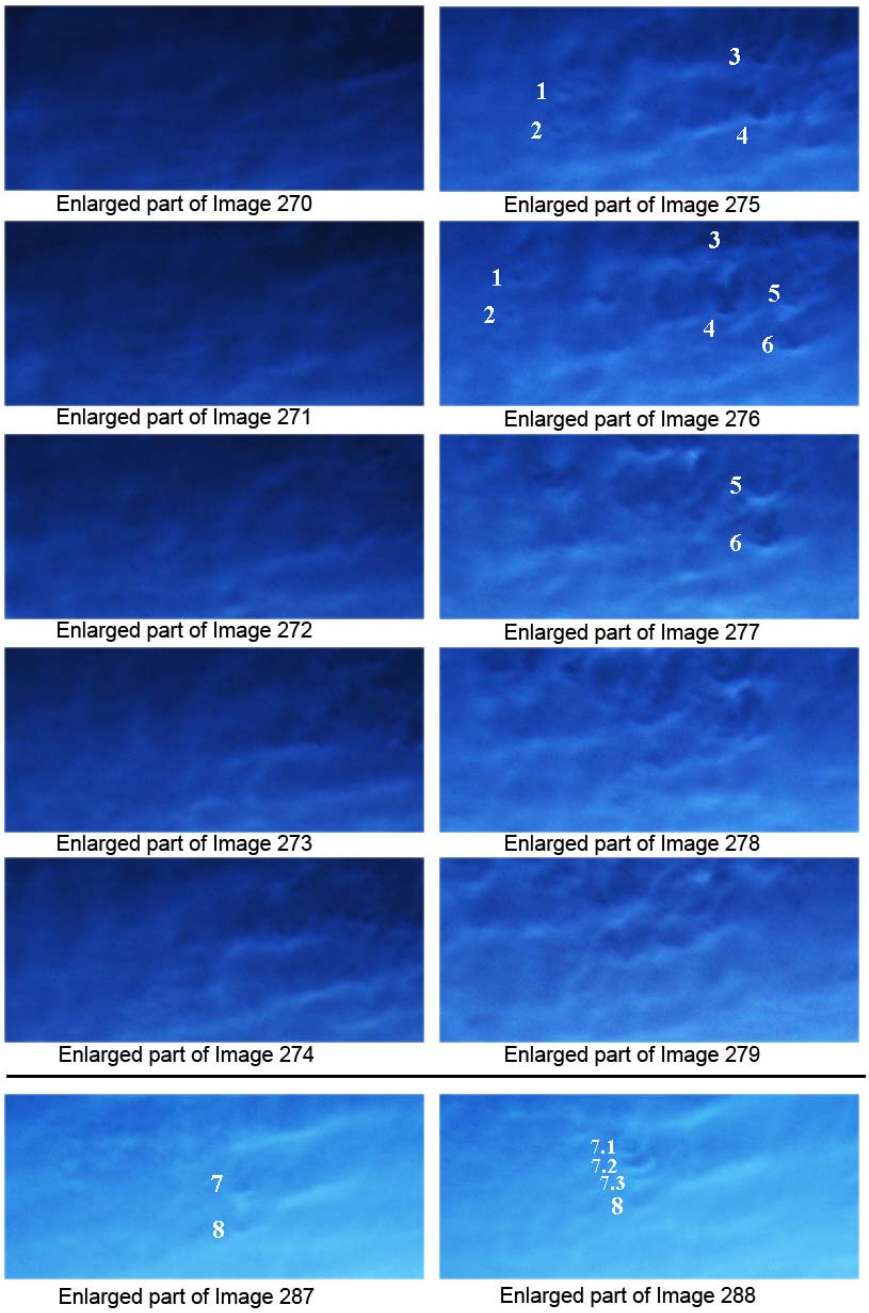

Plate 2. Evolution of the Kelvin-Helmholtz wave in noctilucent clouds. Image 270 is taken at 03:14 local time on 4 July 2008, and subsequent images are taken at 1 minute intervals. Two small-scale holes are marked by 1 and 2 in Images 275 and 276; their diameter is in the range of 800 and 1400 meters. Two larger holes (bounded by horseshoe-like loops) are marked by 3 and 4 in Images 275 and 276; their diameter in Image 275 is 1650 m and 2400 m, respectively. Two largest horseshoe-like loops are marked by 5 and 6 in Images 276 and 277; their diameter in Image 277 is 3550 m and 4600 m, respectively. The horseshoe-like structures are marked by 7 and 8 in Images 287 and 288. The structure 7 is represented by the cascade or packet of the three horseshoe structures marked by 7.1, 7.2, 7.3 in Image 288; diameter of the loops 7.1, 7.2 and 7.3 is 2150 m, 3100m and 3300 m, respectively. The distance between the necks of the horseshoe vortices is in the range of 2800 and 3050 meters.

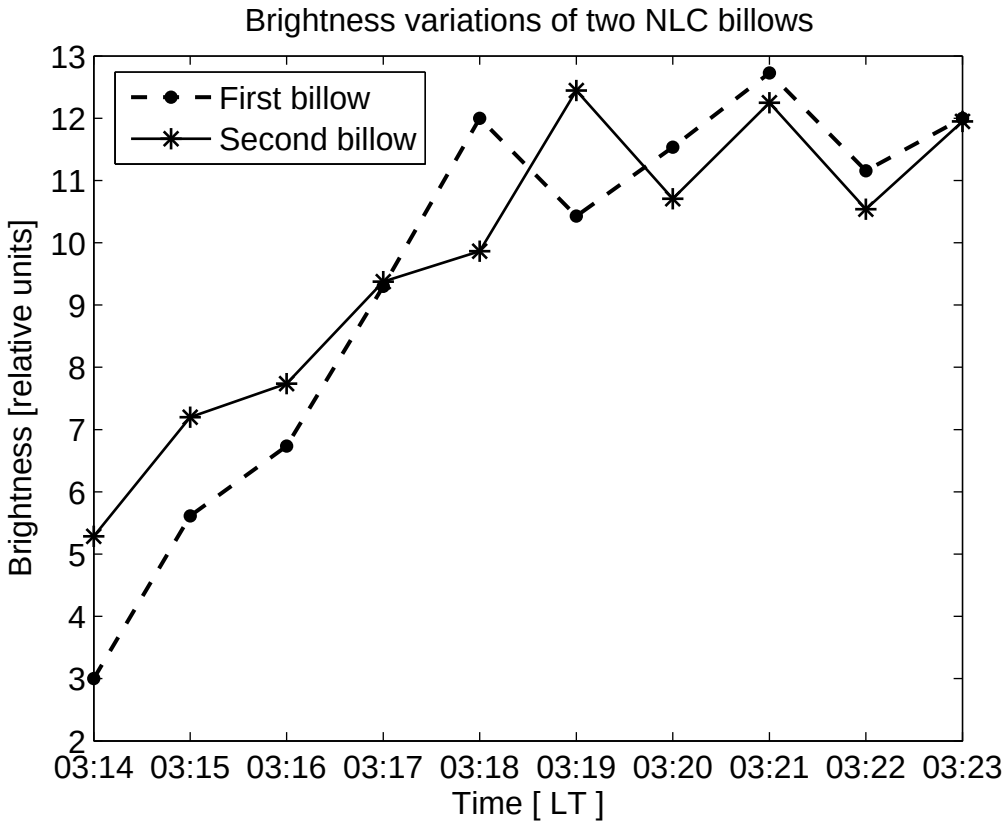

Fig. 2. Brightness variation (after subtracting the background) of the most pronounced two NLC billows seen in images 270-279.

Another set of similar KH waves has been observed in Images 280-290 (not shown except Images 287 and 288, Plate 2). It is important is that the second system of billows has been generated and located in the area of the mesosphere (relative to the ground) where the first one was observed. Again, similar two horseshoe-like loops (marked by 7 and 8) are observed in Images 287 and 288, 12 minutes after the first ones seen in Images 275 and 276. This confirms that there was a steady shear layer in the given area of the mesosphere, generating the KH wave and successive turbulence. The projection on the ground of the KH wave, small holes, jets, arcs seen in Images 275 and 276 is shown in Fig. 3.

We cannot estimate the parameters of vertical wind shear, but we presume its presence from analogy with the KH billows in tropospheric clouds, that commonly occur in the presence of vertical wind shears. The presence of vertical wind shear in NLCs is confirmed by the occurrence of horseshoe-like structures, which are 3D objects and are naturally inclined at 30-60 degrees to a main flow (Adrian, 2000). The horseshoe-shaped turbulent vortices are seen in Images 275-279, as well as the cascade of the horseshoe-shaped vortices arranged in the streamwise direction (7.1, 7.2, 7.3) is evident in Images 287 and 288. Description of these structures is given in the Discussion.

5. Analysis and characteristics of turbulent areas in NLC

Now we want the reader to pay attention to another NLC feature seen at the vicinity of the KH wave. Images 275 and 276 on Plate 2 (and their repeatedly enlarged parts on Plate 3)

demonstrate not only the large holes on the top of the billow waves but also two smaller holes (marked by 1 and 2 on Plates 2 and 3 and in Fig. 3) located slightly away (to the left) from the sharp (well identified) parts of the billows. At the same time, a closer inspection of the images reveals that these holes are still placed on the degraded parts of the wave crests. Note that the large holes and small holes are of similar origin, that is these are turbulent vortexes; but the strength of vorticity, that is the perturbation vorticity and perturbation velocities (and in turn, density and temperature disturbances) in these structures are different. This results in different dynamics of the large and small holes.

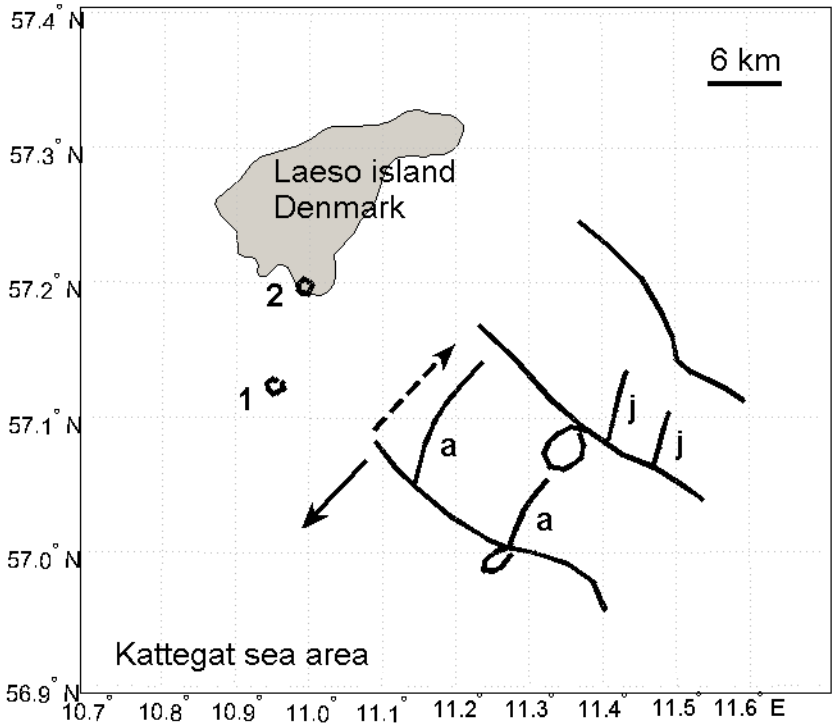

Fig. 3. Projection of the KH wave on the Earth's surface; two holes on the top of the crests are indicated, two smaller holes (marked by 1 and 2) are slightly apart from the wave; two jets and two arcs seen in NLC in Image 275 and 276 are marked by *j* and *a*, respectively. The solid arrow indicates the apparent direction of the wave billows; the dashed arrow shows the direction of the wave billows relative to ambient NLC areas.

A rather large uncertainty in determining the position of the boundaries of fine structures of NLC comes from the movement of fine structures at a high velocity of about 100 m/s and from rather long 8-second exposure time; these factors tend to smear out the boundaries of small-scale features. Nevertheless it is still possible to define the boundaries by tracing the pixels of equal brightness in the middle of the smeared boundary of a fine structure.

The small holes can be represented either by turbulent eddies or by cellular convection. It would be possible to speculate about the cellular convection (cellular convective areas) but such phenomenon is of different scales in the mesosphere, with cells from 10 km and larger in radius (Trubnikov and Skuratova, 1967). In present case we deal with small holes which are less than 700 meters in radius. Also, please note that no well-defined cellular convective filed has

been observed in the NLC images (as it is usually seen in tropospheric clouds), there have occurred a few numbers of sporadic turbulent holes in the NLC layer.

In the case of turbulent eddies, turbulent motions of the NLC surrounding areas around a hole should disperse the bounds of a hole, and a small hole will be reduced in size and even closed. The physics of this process is the same as that responsible for dispersion of artificial clouds in the mesosphere (a cloud of chemical release or cloud of metalized chaff). The summary of these techniques is well described by Lübken (1993). But the behavior of a dispersed cloud and a hole is different: while the former grows in size, the latter is reduced. Indeed Images 275 and 276 (see their enlarged parts in Plate 3) illustrate that the holes are shrinking and completely disappear in Image 277.

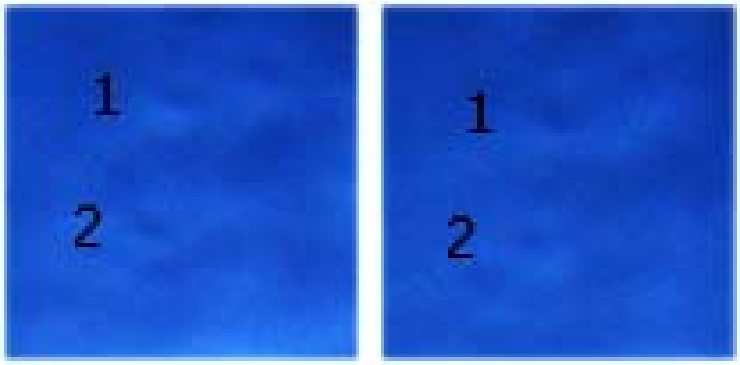

Plate 3. Repeatedly enlarged part of Image 275 and 276 with two small holes. Small-scale holes analyzed are marked by 1 and 2.

There can be three reasons responsible for observed hole shrinking. The first one is a turbulent motion of the surrounding boundaries of the hole; the second one is the wave motion; the third one is the formation of new ice particles. However, the third process does not contribute much because growth rate of ice particles is too slow (the rate of change of radius of a spherical particle is 3.08×10^{-12} m/s, Gadsden and Schröder, 1989) and it takes about 10 hours for a particle to grow to a radius of about 100 nm, but in present case we deal with times of two-three minutes. Therefore next we consider the first two processes.

5.1 Turbulent diffusion at large scales beyond the inertial subrange of the turbulent spectrum

Let's suppose the decreasing area of the hole is solely controlled by the turbulent diffusion of ice particles of the surrounding areas. Then for the turbulent motions at large scales beyond the inertial subrange (approximately 10-200 meters in the middle atmosphere), the time dependence of the cloud radius (or hole radius), $\sigma(t)$, is described as follows (Batchelor, 1950; Lübken, 1993):

$$\sigma^2(t) = 4 \cdot K_1 \cdot t \qquad (1)$$

where K_1 is the turbulent diffusion coefficient. For 1 minute (between Images 275 and 276) the radius of the first and second hole is decreased from 700 to 500 meters and from 550 to 400 meters, respectively. Even if Eq. (1) is applicable to the decrease of the area of the hole, it would yield diffusion coefficients of 1000 m^2/s and 594 m^2/s, respectively. Indeed, these values are too large compared to experimental and theoretical estimations of the turbulent diffusion coefficient

in the summer mesosphere ranging between 2 and 200 m^2/s (Thrane et al., 1985; Lübken, 1997; Gavrilov and Jacobi, 2004). It has been noted by Lübken (1993) that "…non-turbulent processes, such small-scale gravity waves and wind shears, may contribute to the observed cloud dispersion". In this case one needs to redefine the time dependence of the radius of the hole in the following way:

$$\sigma^2(t) = 4 \cdot K_1 \cdot t \pm r^2(t) \qquad (2.1)$$

where *r(t)* is the hole radius changing due to non-turbulent process; plus and minus sign corresponds to the decrease and increase of the area of the hole, respectively. As will be shown below, we deal with the decrease of the area of the hole due to non-turbulent process and therefore we keep the plus sign only in the successive analysis. It is more convenient (for further consideration) to rewrite Eq. (2.1) in the form of:

$$S(t) = 4 \cdot \pi \cdot K_1 \cdot t + S_n(t) \qquad (2.2)$$

where $S(t)$ is the measured decreasing of the area of the hole, $S_n(t)$ is the decreasing of the area of the hole due to non-turbulent processes.

The presence of the non-turbulent motion can be inferred from measuring the distance between the centers of the observed two holes. Images 275 and 276 provide information on the distance between the centers of the holes which is decreased from 8.39 km to 7.34 km in 1 minute time interval. From this one can deduce the mutual speed of the holes' motion (perpendicular to the wave phase front) which is equal to 17.5 m/s.

If we suppose that such a speed is equal to the difference of speeds of opposite sides of a hole due to the difference in speeds at the leading edge of a local sudden wind gust, this would lead to a decrease of the area of a hole; the first hole of approximately 1.4 km in diameter would completely disappear in less than 1.5 minute, and the second hole of 1.1 km in diameter would disappear in about 1 minute. But the two holes exist during at least 1 minute without dramatic decrease of the area. Thus, local wind gusts cannot be a reason for decreasing the size of the holes in the present case.

On the other hand, one can suggest that the speed of 17.5 m/s is the mutual speed difference of two points (separated by ~8 km) in sinusoidal horizontal velocity perturbation of a gravity wave. The wavelength of the regarded wave is 10-12 km, and the velocity amplitude is likely about 10 m/s, which is in the range of amplitude velocities of short period gravity waves in the summer mesosphere (Manson et al., 1981; Reid and Vincent, 1987; Manson et al., 2004). In this case, one can expect that two points of the wave separated by 1.1-1.4 km (the diameters of the holes) could have the mutual speed difference in the range of 1-7 m/s depending on the phase difference; on average, one can assume speeds of 3-5 m/s. One can consider the decrease of the area of the hole as due to the moving of one semi-circle to another one (Fig. 4). Such a consideration is supported by the observational fact that the first and second holes have an elliptical form with eccentricity of 0.45 and 0.63, respectively, with major axes being oriented approximately perpendicular to the direction of the mutual moving of semi-circles.

Then a simple geometrical consideration provides the following equation for decreasing of the area of the segment (the hatched area in Fig. 4) between two semi-circles:

$$S_n(t) = \pi \cdot R^2 - 2 \cdot (R^2 \cdot \arccos((R - h(t))/R) - (R - h(t)) \cdot \sqrt{2 \cdot R \cdot h(t) - h^2(t)}) \qquad (3.1)$$

where

$$h(t) = (2 \cdot R - x(t))/2 \qquad (3.2)$$

$$x(t) = v \cdot t \qquad (3.3)$$

where R is the radius of the semi-circles (that is the initial radius of the hole), v is the speed of one semi-circle relative to another one, t is the time elapsed from beginning of the approach. As the initial radius we take the average radius of the first and second hole of 700 and 550 m, respectively, (measured in Image 275), speed of 3-5 m/s (assumed above) and time of 60 seconds (between the two successive images). Then Eqs. (3.1-3.3) yield the decrease the area of the first and second hole in the range of $2.5 \cdot 10^5$ - $4.2 \cdot 10^5$ m^2, and of $2.0 \cdot 10^5$ - $3.3 \cdot 10^5$ m^2, respectively, due to non-turbulent process. By using Eq. (2.2) and subtracting these values from the measured decreasing of the square of the holes, one can obtain the turbulent diffusion coefficients (K_1) in the range of 447-667 m^2/s for the first hole and of 162-332 m^2/s for the second hole. These values are rather close to and even partly within the range of values of the turbulent diffusion coefficient reported in previous studies.

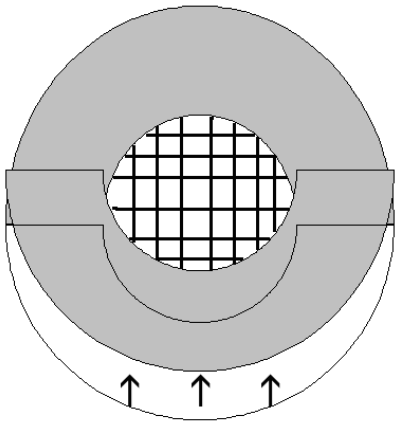

Fig. 4. Schematic picture of the observed hole represented by two semi-circles; the lower semi-circle moves to the upper one. The hatched area is the square of the segment estimated.

5.2 Turbulent diffusion at medium scales of the turbulent spectrum

Now we regard scales between 400 and 700 meters which can also be attributed to the inertial subrange of the turbulent spectrum in the middle atmosphere, limits of that are poorly known and can vary. In this case, the cloud radius changes as (Lübken (1993)):

$$\sigma^2(t) = c \cdot \varepsilon \cdot t^3$$

where c≈0.6 is a constant and ε is the turbulent energy dissipation rate. From this relation, one can estimate ε which is equal to:

- for the first hole (from 700 to 500 m): ε=828-1235 mW/kg for the wave motion subtracted, and 1852 mW/kg for no wave motion;
- for the second hole (from 550 to 400 m): ε=300-615 mW/kg for the wave motion subtracted, and 1100 mW/kg for no wave motion.

Then the turbulent diffusion coefficient for the transition range between the inertial subrange and larger scales is determined as follows:

$$K_2 = c_1 \cdot \varepsilon^{1/3} \cdot l^{4/3}$$

where $c_1 \approx 1$ is a constant, and l is the scale of diffusion.

This relation yields the following estimations of K_2:

- for the first hole (from 700 to 500 m): K_2=1098-1255 m^2/s, with wave motion subtracted.
- for the second hole (from 550 to 400 m): K_2=533-677 m^2/s, with wave motion subtracted.

One can see that the K_2 values are larger than K_1 values; the same effect was described by Lübken (1993) and the author noted "The ε values were therefore empirically reduced so that K_2 agrees with K_1".

Thus, for the present case, the dependence of the hole radius change is described better (a value of the turbulent diffusion coefficient is less) if the turbulent diffusion is considered at larger scales beyond the inertial subrange.

6. Discussion

We have considered a unique case of the NLC display observed from Denmark. The unique case is due to the occurrence of bright and extensive NLC at high elevation angles (more than 30 degrees) as well as the observations of the evolution of the KH wave and the subsequent transition to turbulence. The KH wave evolution resembles the laboratory experiment on the KH wave performed by Thorpe (1971), and turbulent regime resembles the turbulent field and vorticity structures in 3-D simulations of the evolution of the KH wave (by Palmer et al., 1996; Werne and Fritts, 2001).

In general, both laboratory and modeling studies demonstrate very similar behavior of the initial and main phase of the KH evolution. Major differences in 3-D KH simulations occur during transitions to turbulence (Fritts and Alexander, 2003). In our case we have observed small turbulent areas (holes), fragmentized KH billows and splintered curves, large lacerated dark turbulent areas and horseshoe-shaped coherent eddies.

Small turbulent holes (of about 1-1.4 km in diameter) have been formed within or close to the KH billows. By size estimations of turbulent areas the turbulent diffusion coefficient can be deduced. At the same time, it has been demonstrated that it is of importance to take into account non-turbulent process such as the gravity wave motion that is always present in NLC layers. Unless non-turbulent process is taken into account, this certainly leads to overestimation of the value of the turbulent diffusion coefficient. In the present study, we do not insist on a quantitatively correct estimation of the turbulent diffusion coefficient (it is not possible due to low spatial and temporal resolution of present data) but we demonstrate such a principal possibility for estimating of the turbulent diffusion based on a series of NLC images with evolving small-scale eddies. More precise estimation will be done in future with high resolution (in space and time) images.

Watkins et al. (1988) estimated turbulence energy dissipation rates using simultaneous rocket and radar data from the STATE experiment and found typical values in the range of 50-150 mW/kg, with one case (15 June 1983) of very strong neutral turbulence being equal to about 1000 mW/kg at 87 km. Such intense turbulence lasted a few minutes but still was clearly presented in the data. Please note that authors registered a high level of turbulence with ε more than 200 mW/kg at 85 km for another case on 16 June 1983, and such large values sustained for a long period of about 4 hours. The essential point is that most intense turbulence is observed in regions where wave field and amplitudes are unstable (Fritts et al., 1988). We do observe turbulent structures in the vicinity of breaking small-scale gravity waves that seems to be responsible for a high level of turbulence.

Lübken (1993) demonstrated the following measured turbulent parameters around the summer mesopause (page 139). On 9 Aug 1991, between 82-84 km, the turbulent energy dissipation rate (ε) was about 0.4 mW/kg. For another case, 1 Aug 1991, with strong PMSE between 84-91 km, ε was about 3 mW/kg for the altitude range of 82-83 km. For another experiment on 28 July 1993, Lübken et al. (1994) showed strong neutral air turbulence with

436 ε=630 mW/kg inside a PMSE layer between 84.5-85.5 km. This ε-value perfectly matches our
437 estimations of ε of 300-615 mW/kg for the second small hole. Thus, one can conclude that the
438 turbulent energy dissipation rate can change significantly by three orders of magnitude between
439 82 and 85 km, that is exactly the NLC altitude range. Since $K \sim \varepsilon^{1/3}$ for the inertial subrange, K
440 can readily change and increase by a factor of 10 in a case of strong turbulence, which probably
441 took place in the present case study.
442 Horseshoe- or hairpin-like structures have been studied by direct numerical simulations (Gerz
443 et al., 1994) and with experimental observations (Head and Bandyopadhyay, 1981; Adrian et al.,
444 2000). The horseshoe vortex is a simple coherent vorticity that develops due to stretching and
445 rotation by the mean shear rate. These are 3D structures which are usually inclined at 30-60
446 degrees to a main flow (Adrian et al., 2000). Such a vortex represents the dynamically most
447 active parts of the sheared turbulent flow, since it controls the fluxes of momentum, heat and
448 species (Gerz et al., 1994). The head, necks and legs are usually supposed to discern in the
449 hairpin- or horseshoe-like structure. In our case the legs of such a structure are hardly visible, but
450 the head and necks are clearly seen in Images 275-279 as well as in 287 and 288. The distance
451 between the necks of the horseshoe vortices (the diameter of the visible loops) varies in the range
452 between 1650 and 4600 meters. Image 288 demonstrates one more interesting feature, namely the
453 cascade or packet of the three horseshoe structures (marked by 7.1, 7.2, 7.3) oriented in the
454 streamwise direction; diameter of the loops 7.1, 7.2 and 7.3 is 2150 m, 3100m and 3300 m,
455 respectively. Adrian et al. (2000) have observed similar coherently (spatially) arranged vortical
456 structures, spaced typically several hundred viscous lengthscales apart in the streamwise
457 direction. In our case the viscous lengthscale in the environment of the shear layer and horseshoe
458 structures is of the order of 10 m (estimated as the ratio of the kinematic viscosity to the friction
459 velocity) and the distance between the heads of these structures is 3050 and 2800 m; thus the
460 observed distance between the NLC horseshoe structures in the packet perfectly matches the
461 distance between hairpin-like structures in the packet found in the laboratory experiment by
462 Adrian et al. (2000).
463 As a rule, hairpin vortices occur in fully developed wall-bounded turbulent shear flows
464 Suponitsky et al. (2005). However, it is not a necessary and sufficient condition. The authors
465 performed model studies and clearly demonstrated that the coherent structures (streaks and
466 hairpin/horseshoe vortices) can form and evolve in a laminar uniform unbounded shear flow. The
467 authors noted: “The common elements for all such flows are the shear of the base flow and the
468 presence of a localized vortical disturbance.” The KH instability forms under the presence of a
469 shear layer. Also, we demonstrate the region containing both breaking KH waves and signatures
470 of a turbulent flow (lacerated unformed structures and spots, small-scale holes/eddies, horseshoes
471 vortices and even a cascade of horseshoes vortices). It requires, at least, a region around the
472 mesopause filled with a shear layer and localized small-scale vortical disturbances.
473 Similar fine horseshoe-like structures in NLC were captured recently on July 13/14 and 14/15
474 of 2009 during exceptional NLC displays in Lithuania from two points with cameras operating in
475 synchronous shooting regime. The data analysis is in progress and will allow 3D recovery of the
476 turbulent characteristics.
477 Note that we consider a simple mechanistic approach considering the dynamics of the holes
478 photographed with low spatial (~135 meters), low temporal resolution (60 seconds) and with
479 rather long 8-second exposure time (that leads to smearing out the boundaries), but even such a
480 simple approach provides reasonable estimates of the turbulent diffusion coefficient when the
481 gravity wave motion is taken into account. More accurate estimates can be obtained by analysing

the sequence of successive images taken at short exposure times (1-2 seconds), with high temporal (of 5 seconds) and spatial resolution (of 10 meters), that is relatively easy to achieve by using modern commercial digital cameras of more than 5 Mp and with a teleobjective with a focal length of about 150 mm. In this case one can measure more precisely the size of turbulent areas in NLC as well as input of the wave motion, and finally deduce the time dependence of the turbulent process at different scales. Such a technique will be used in the future to study turbulent areas in NLC at high elevation angles.

Also, a particular interest is to resolve the formation of turbulent areas from the very beginning, which seem to occur rather fast in less than one minute or maybe even during several seconds. For this the temporal resolution of 1 second is required, that is possible to achieve with high sensitivity and high frame rate digital cameras produced for industrial and scientific purposes. This technique is of low cost compared to other techniques applied for studies of turbulent regime in the middle atmosphere.

7. Conclusions

We can summarize the following. A local wind shear had occurred around the mesopause which excited a series of Kelvin-Helmholtz waves seen in noctilucent clouds. The billows had wavelength of 10-12 km and lifetime of 6-7 minutes. The billow evolution led to the formation of turbulent area with a mixture of the splintered curves, large lacerated dark areas as well horseshoe-shaped vortical coherent structures of 1.5-3.5 km in diameter.

There were created pairs of very small turbulent holes of about 1-1.5 km in diameter which were covered by NLC surrounding areas in 2 minutes. This allowed us to estimate the turbulent diffusion coefficient (taking into account non-turbulent process) in the range of 162-667 m^2/s and the turbulent energy dissipation rate of 300-1235 mW/kg. These values are rather close and partly within the range of turbulent parameters inferred from previous experimental and theoretical studies (2-200 m^2/s and 0.1-1000 mW/kg) for the summer mesosphere, and represent a case of strong neutral air turbulence in the vicinity of breaking small-scale gravity waves in noctilucent clouds.

Acknowledgements

We acknowledge Prof. S.A. Thorpe, Journal of Fluid Mechanics and Cambridge University Press for permission to reproduce Fig. 5 from the article by Thorpe, S.A., 1971, Experiments on the instability of stratified shear flows: miscible fluids, Journal of Fluid Mechanics", vol. 46, part 2, pp. 299-319. The paper benefited from constructive comments and suggestions made by Editor Markus Rapp and one anonymous reviewer.

References

Adrian, R.J., Meinhart, C.D., and Tomkins, C.D., 2000. Vortex organization in the outer region of the turbulent boundary layer. Journal of Fluid Mechanics 422, 1-54.

Burov, M.I., 1959. Methode photogrammetrique pour la determination de l'altitude des nuages argents. (in Russian), Trudy soveschaniya po serebristym oblakam, Tartu, 92–111.

Burov, M.I., 1967. Spatial and dynamic characteristics of noctilucent clouds. Noctilucent Clouds International Symposium, Tallinn, VINITI, ed. by I. A. Khvostikov and G. Witt, 200-207.

528 Batchelor, G.K., 1950. The application of the similarity theory of turbulence to atmospheric
529 diffusion. Quarterly Journal of the Royal Meteorological Society 76, 133-146.
530 Browand, F.K., and Winant, C.D., 1973. Laboratory observations of shear-layer instability in a
531 stratified fluid. Boundary-Layer Meteorology 5, 67-77.
532 Browning, K.A., and Watkins, C.D., 1970. Observations of clear air turbulence by high power
533 radar. Nature 227, 260-263.
534 Corcos, G., and Sherman, F., 1976. Vorticity concentration and the dynamics of unstable free
535 shear layers. Journal of Fluid Mechanics 73, 241–264.
536 Dalin, P., Kirkwood, S., Moström, A., Stebel, K., Hoffmann, P., Singer, W., 2004. A case study
537 of gravity waves in noctilucent clouds. Annales Geophysicae 22, 1875-1884.
538 Dalin, P., Pertsev, N., Zadorozhny, A., Connors, M., Schofield, I., Shelton, I., Zalcik, M.,
539 McEwan, T., McEachran, I., Frandsen, S., Hansen, O., Andersen, H., Sukhodoev, V.,
540 Perminov, V., Romejko, V., 2008. Ground-based observations of noctilucent clouds with a
541 northern hemisphere network of automatic digital cameras. Journal of Atmospheric and
542 Solar-Terrestrial Physics 70, 1460-1472, doi:10.1016/j.jastp.2008.04.018.
543 Drazin, P.G., 1970. Kelvin-Helmholtz instability of finite amplitude. Journal of Fluid Mechanics
544 42, 321-335.
545 Fritts, D.C., 1982. Shear excitation of atmospheric gravity waves. Journal of the Atmospheric
546 Sciences 39, 1936-1952.
547 Fritts, D.C., and Rastogi, P.K., 1985. Convective and dynamical instabilities due to gravity wave
548 motions in the lower and middle atmosphere: theory and observations. Radio Science 20 (6),
549 1247-1277.
550 Fritts, D.C., Smith, S.A., Balsley, B.B., and Philbrick, C.R., 1988. Evidence of gravity wave
551 saturation and local turbulence production in the summer mesosphere and lower
552 thermosphere during the STATE experiment. Journal of Geophysical Research 93 (D6),
553 7015-7025.
554 Fritts, D.C., and Alexander, M.J., 2003. Gravity wave dynamics and effects in the middle
555 atmosphere. Reviews of Geophysics 41 (1),1003, doi:10.1029/2001RG000106.
556 Gadsden, M, and Schröder, W., 1989. Noctilucent clouds, Springer-Verlag, Berlin.
557 Gavrilov, N.M, and Jacobi, Ch., 2004. A study of seasonal variations of gravity wave intensity in
558 the lower thermosphere using LF D1 wind observations and a numerical model. Annales
559 Geophysicae 22, 35-45.
560 Gerz, T., Howell, J., and Mahrt, L., 1994. Vortex structures and microfronts. Physics of Fluids 6
561 (3), 1242-1251.
562 Grishin, N.I., and Kurilova, J.V., 1973. Morphology and dynamics of noctilucent clouds.
563 Noctilucent clouds. Optical properties, Akademia Nauk, Tallinn, pp. 56.
564 Gossard, E.E., Jensen, D.R., and Richter, J.H., 1971. An analytic study of tropospheric structure
565 as seen by high-resolution radar. Journal of the Atmospheric Sciences 28, 794-807.
566 Haurwitz, B., and Fogle, B., 1969. Wave forms in noctilucent clouds. Deep-Sea Research 16, 85-95.
567 Head, M.R., and Bandyopadhyay, P., 1981. New aspects of turbulence boundary-layer structure.
568 Journal of Fluid Mechanics 107, 297-338.
569 Hicks, J.J., and Angell, J.K., 1968. Radar observations of breaking gravitational waves in the
570 visually clear atmosphere. Journal of Applied Meteorology 7, 114-121.
571 Hines, C.O., 1968. A possible source of waves in noctilucent clouds. Journal of the Atmospheric
572 Sciences 25, 937-942.
573 Kelly, R.E., and Maslowe, S.A., 1970. The nonlinear critical layer in a slightly stratified shear
574 flow. Studies in Applied Mathematics 49, 301-326.

575 Kuhnke, F., 1976. Leuchtende Nachtwolken als Indikator für Wellenerscheinungen in der
576 Mesopause. Dipl-Arbeit, Univ. Braunschweig.
577 Ludlam, F.H., 1967. Billow clouds and their relation to clear air turbulence. Quarterly Journal of
578 the Royal Meteorological Society 93, 419-435.
579 Lübken, F.-J., 1993. Experimental results on the role of turbulence for the heat budget of the
580 upper atmosphere. Bonn University, Bonn-IR-93-51.
581 Lübken, F.-J., Giebeler, J., Blix, T., Thrane, E., Singer, W., and Bremer, J., 1994. In-situ
582 measurements of the Schmidt number within a PMSE layer. Geophysical Research Letters 21
583 (15), 1651-1654.
584 Lübken, F.-J., 1997. Seasonal variation of turbulent energy dissipation rates at high latitudes as
585 determined by in situ measurements of neutral density fluctuations. Journal of Geophysical
586 Research 102, 13441-13456.
587 Manson, A.H., Meek, C.E., Gregory, J.B., 1981. Gravity waves of short period (5-90 min), in the
588 lower thermosphere at 52°N (Saskatoon, Canada); 1978/1979. Journal of Atmospheric and
589 Terrestrial Physics 43, 35-44.
590 Manson, A.H., Meek, C.E., Chshyolkova, T., Avery, S.K., Thorsen, D., MacDougall, J.W.,
591 Hocking, W., Murayama, Y., Igarashi, K., Namboothiri, S.P., Kishore, P., 2004. Longitudinal
592 and latitudinal variations in dynamic characteristics of the MLT (70-95 km): a study
593 involving the CUJO network. Annales Geophysicae 22, 347-365.
594 Nussbaumer, V., Fricke, K.-H., Langer, M., Singer, W., and von Zahn, U., 1996. First
595 simultaneous and common volume observations of noctilucent clouds and polar mesosphere
596 summer echoes by lidar and radar. Journal of Geophysical Research 101, 19,161–19,167.
597 Palmer, T.L., Fritts, D.C., Andreassen, Ø., 1996. Evolution and breakdown of Kelvin-Helmholtz
598 billows in stratified compressible flows. Part II: instability structures, evolution, and
599 energetics. Journal of the Atmospheric Sciences 53 (22), 3192-3212.
600 Patnaik, P.C., Sherman, F.S., and Corcos, G.M., 1976. A numerical simulation of Kelvin-
601 Helmholtz waves of finite amplitude. Journal of Fluid Mechanics 73, 215-240.
602 Peltier, W.R., Hallé, J.R. and Clark, T.L., 1978. The evolution of finite amplitude Kelvin-
603 Helmholtz billows. Geophysical & Astrophysical Fluid Dynamics 10, 53-87.
604 Reid, I.M., and Vincent R.A., 1987. Measurements of the horizontal scales and phase velocities
605 of short period mesospheric gravity waves at Adelaide, Australia. Journal of Atmospheric and
606 Terrestrial Physics 49 (10), 1033-1048.
607 Scotti, R.S., and Corcos, G.M., 1972. An experiment on the stability of small disturbances in a
608 stratified free shear layer. Journal of Fluid Mechanics 52, 499-528.
609 Suponitsky, V., Cohen, J., and Bar-Yoseph, P.Z., 2005. The generation of streaks and hairpin
610 vortices from a localized vortex disturbance embedded in unbounded uniform shear flow.
611 Journal of Fluid Mechanics 535, 65-100, doi:10.1017/S0022112005004453.
612 Tanaka, H., 1975. Quasi-linear and nonlinear interactions of finite amplitude perturbations in a
613 stably stratified fluid with hyperbolic tangent shear. Journal of the Meteorological Society of
614 Japan 53, 1-32.
615 Thorpe, S.A., 1968. A method of producing a shear flow in a stratified fluid. Journal of Fluid
616 Mechanics 32, 693-704.
617 Thorpe, S.A., 1971. Experiments on the instability of stratified shear flows: miscible fluids.
618 Journal of Fluid Mechanics 46 (2), 299-319.
619 Thorpe, S.A., 1973. Experiments on instability and turbulence in a stratified shear flow. Journal
620 of Fluid Mechanics 61, 731-751.

621 Thrane, E.V., Andreassen, Ø., Blix, T., Grandal, B., Brekke, A., Philbrick, C.R., Schmidlin, F.J.,
622 Widdel, H.U., von Zahn, U., Lübken, F.J., 1985. Neutral air turbulence in the upper
623 atmosphere observed during the Energy Budget Campaign. Journal of Atmospheric and
624 Terrestrial Physics 47 (1), 243-264.
625 Trubnikov, B.N., and Skuratova, I.S., 1967. Cellular convection in the zone of noctilucent clouds.
626 Noctilucent clouds, Proceedings of International Symposium, Khvostikov, I.A. and Witt, G.
627 (Eds.), VINITI, Moscow, 208-215.
628 Watkins, B.J., Philbrick, C.R., Balsley, B.B., 1988. Turbulence energy dissipation rates and inner
629 scale sizes from rocket and radar data. Journal of Geophysical Research 93 (D6), 7009-7014.
630 Werne, J., and Fritts, D.C., 2001. Anisotropy in a stratified shear layer. Physics and Chemistry of
631 the Earth 26 (4), 263-268.
632 Witt, G., 1962. Height, structure and displacements of noctilucent clouds. Tellus XIV (1), 1–18.